

Comparison of bar formation mechanisms II: does a tidally forced bar grow faster than an internally developed bar?

YIRUI ZHENG,^{1,2} JUNTAI SHEN,^{1,2} XUFEN WU,^{3,4} AND BIN-HUI CHEN^{5,1,2}

¹*Department of Astronomy, School of Physics and Astronomy, Shanghai Jiao Tong University, 800 Dongchuan Road, Shanghai 200240, P.R. China*

²*National Key Laboratory of Dark Matter Physics / Shanghai Key Laboratory for Particle Physics and Cosmology, Shanghai 200240, P.R. China*

³*Department of Astronomy, University of Science and Technology of China, Hefei, 230026, P.R. China*

⁴*School of Astronomy and Space Science, University of Science and Technology of China, Hefei 230026, P.R. China*

⁵*Tsung-Dao Lee Institute, Shanghai Jiao Tong University, Shanghai 200240, People's Republic of China*

ABSTRACT

Bar structures can form internally due to the instability of their host galaxies or externally due to perturbations from other galaxies. We systematically quantify the growth timescales (τ_{bar}) of bars formed through these two mechanisms with a series of controlled N -body simulations. In galaxies susceptible to bar instability, tidally forced bars display τ_{bar} values comparable to those of internally developed bars within the same disk. Tidal perturbations promote/delay bar formation by advancing/postponing its onset, but the growth rate of the bar structure remains largely unchanged. In these interaction scenarios, the bar formation is still driven primarily by the galaxy's internal nature that remains unaffected by tidal perturbations. As the external perturbation wave reaches the galaxy's center, it evokes a “seed bar” that is then swing amplified. In this scenario, the onset of bar formation is advanced. Conversely, bar formation may be delayed if the external perturbation wave is out of phase with the pre-existing spontaneously developed seed bar, which causes destructive interference and limits the bar growth. In the hot disk model that resists bar formation in isolation, τ_{bar} of the tidally forced bar correlates with the strength of the perturbation. The bar growth in this model deviates from the exponential profile and is better described by a linear function. The varied τ_{bar} and the preference for linear growth contrast with bars formed in galaxies inherently susceptible to bar instability. These tidally forced bars may not adhere to the swing amplification mechanism that predicts an exponential bar growth.

Keywords: galaxies: kinematics and dynamics — galaxies: structures

1. INTRODUCTION

Bars are a common feature in spiral galaxies. Locally, about half of the disk galaxies possess bars in optical bands, with this proportion rising to two-thirds in infrared bands (Marinova & Jogee 2007; Menéndez-Delmestre et al. 2007; Erwin 2018; Lee et al. 2019). Although a smaller fraction of galaxies have bars at higher redshifts, they still represent 13% in the range $2 < z \leq 3$ (Le Conte et al. 2024) and appear as early as $z \sim 4$ (Guo et al. 2024). Bars significantly influence the evolution

of their host galaxies, including triggering gas inflow, affecting star formation, and contributing to the formation of pseudo-bulges (Masters et al. 2011; Li et al. 2015; Lin et al. 2017, 2020; Iles et al. 2022). The Milky Way also has a bar (e.g. de Vaucouleurs 1964; Blitz & Spergel 1991), and its boxy-bulge and gas dynamics are directly linked to this bar (e.g. Shen et al. 2010; Li et al. 2018). The prevalence and impact of bars on galaxies highlight the importance of studying their formation and evolution.

Galactic bars can form via internal or external mechanisms. Internally, bars can develop spontaneously due to the gravitational instability of the disks (Hohl 1971; Ostriker & Peebles 1973; Sellwood 2014; Lokas 2019a).

A widely recognized mechanism for spontaneous bar formation is the swing amplification loop, initially developed by Goldreich & Lynden-Bell (1965) and Julian & Toomre (1966) and further elaborated by Toomre (1981). Binney (2020) revisited this concept and provided a more accessible explanation. According to this model, any source of noise generates a packet of leading spiral waves, which are then amplified as they swing from leading to trailing. The amplified trailing waves propagate through the disk center and reemerge as a leading disturbance, which then triggers the next swing amplification loop. The repeated amplification process amplifies minor noise into a prominent spiral pattern and ultimately facilitates the formation of a coherent bar. The positive feedback loop predicts exponential growth of the spiral/bar strength.

Several studies investigated the growth rate or equivalently the formation timescale of bars formed via internal instability. The formation timescale is found to depend on the bulge-to-disk mass fraction (Kataria & Das 2018), the Toomre Q parameter (Hozumi 2022; Worakitpoonpon 2024), and the disk thickness (Ghosh et al. 2023). Fujii et al. (2018) found an exponentially decreasing relation between the bar formation timescale and increasing disk mass fraction. The “Fujii relation” was then confirmed in Bland-Hawthorn et al. (2023). An important improvement in the latter work is the quantification of the exponential growth timescale associated with the swing amplification loop instead of Fujii’s fixed threshold for when a bar appears ($A_{2,max} > 0.2$). Bland-Hawthorn et al. (2023) demonstrated that an exponential fit to the growth of A_2 over time provides a timescale and an onset time and also reproduces the Fujii relation independently of any assumptions about A_2 . Several studies have suggested that the disk mass fraction plays a primary role in determining the bar formation timescale (Fujii et al. 2018; Bland-Hawthorn et al. 2023, 2024, 2025). Thus, it is important to control the disk mass fraction when investigating the effects of other parameters on bar formation.

Besides the internal instability, bar formation can also be externally induced by various gravitational perturbations, including flyby encounters with other galaxies, collisions, mergers, or the tidal effects of galaxy clusters (Byrd et al. 1986; Gauthier et al. 2006; Martinez-Valpuesta et al. 2017; Lokas et al. 2016; Lokas 2019b). A comprehensive investigation is desired to compare the growth and evolution of bars formed through different mechanisms. Studies have indicated that tidal interactions can either promote or delay bar formation (Lokas et al. 2016; Moetazedian et al. 2017; Lokas 2018; Pettitt & Wadsley 2018; Zana et al. 2018). This raises a ques-

tion: if tidal forces either promote or delay the formation of bars, do they result in bars that grow at a faster or slower rate compared to those formed internally? Alternatively, do these bars grow at similar rates but onset at different times? Moetazedian et al. (2017) found that the exponential growth rate of tidal bars is independent of the number of satellite encounters and their orbits. However, the rescaled mass of the primary satellite in their simulation is only $< 1\%$ compared to the host halo mass of the galaxy, which limits the strength of the tidal perturbation.

Previous studies have predominantly focused on either the internal or external mechanisms of bar formation, with less attention given to comparing these two mechanisms. In this series of papers, we aim to offer a comprehensive comparison between bars formed through different mechanisms. In Zheng & Shen (2025, Paper I hereafter), we conducted a series of controlled N -body simulations to examine the pattern speed Ω_p of tidally forced bars and compared them with their spontaneous counterparts in the same galaxy model. We found that bars formed via both mechanisms exhibit similar distributions in the pattern speed–bar strength ($\Omega_p - A_2$) space and display comparable ratios of co-rotation radius to bar length ($\mathcal{R} = R_{CR}/R_{bar}$). When “tidally forced bars” refer specifically to those in galaxies stable against bar instability, they indeed rotate slower than internally developed ones in less stable galaxies. However, this difference in pattern speed is attributed to the varying internal properties of the bar host galaxies, rather than the different formation mechanisms. In this second paper, we broaden our investigation to compare the growth timescales and onset times between tidally forced and spontaneously developed bars. Our objective is to understand how external perturbations influence the growth of bar structures.

The structure of the paper is as follows. In Section 2, we provide an overview of the galaxy models and simulation details. Section 3 describes the exponential fitting method used to quantify the bar growth timescale. In Section 4, we present a comparison of the growth timescales and the onset times of bar formation between tidally forced and internally developed bars. The results are interpreted and discussed within the same section. Finally, we conclude with a summary of our findings in Section 5.

2. SIMULATIONS

In this study, we employ the same series of controlled N -body simulations as detailed in Paper I to investigate the bar growth timescale under various mechanisms. For comprehensive details on the simulations, we direct the

reader to [Paper I](#). Here, we offer a concise overview of the simulations' key aspects.

We employ the AGAMA software ([Vasiliev 2019](#)) to generate three galaxy models. These models share a common density profile, differing only in the velocity distribution of their stellar disks. The shared density profile comprises an exponential, quasi-isothermal stellar disk and a truncated Hernquist dark matter (DM) halo. The stellar disk's characteristics include a mass of $M_* = 3.6 \times 10^{10} M_\odot$, a scale length of $R_d = 2$ kpc, and a scale height of $h_z = 0.4$ kpc. The DM halo features a mass of $M_{\text{halo}} = 3.6 \times 10^{11} M_\odot$ and a scale radius of $a = 13.7$ kpc. The combined mass of the stars and DM halo is $M_{\text{tot}} = 4.0 \times 10^{11} M_\odot$.

AGAMA employs an action-based distribution function (DF) to determine the velocity distribution of the stellar disk. We highlight the radial velocity dispersion, a critical physical quantity influencing disk stability. In all disk models, the radial velocity dispersion decreases exponentially with radius, with its scale length being twice that of the density profile, $R_{\sigma,R} = 2 R_d$. By varying the central value of the radial velocity dispersion ($\sigma_{R,0}$) we create three disk models: cold, warm, and hot disks, characterized by $\sigma_{R,0} = 73$ km/s, 124 km/s, and 226 km/s, respectively.

Following [Fujii et al. \(2018\)](#) and [Bland-Hawthorn et al. \(2023\)](#), we calculate the f_{disk} parameter as the ratio of the disk mass to the total galaxy mass within the radius at $R = 2.2 R_d$ at which the rotation curve roughly peaks. f_{disk} is defined by:

$$f_{\text{disk}} = \frac{V_{c,\text{disk}}^2(R)}{V_{c,\text{tot}}^2(R)} \bigg|_{R=2.2 R_d}, \quad (1)$$

with $V_c(R)$ denoting the circular velocity at radius R . The cold, warm, and hot disks have f_{disk} values of 0.47, 0.47, and 0.44, respectively, positioning them within the intermediate disk mass fraction range on the Fujii relation ([Fujii et al. 2018](#); [Bland-Hawthorn et al. 2023](#)).

These models have very similar f_{disk} values, which is an expected outcome of using identical parameters for the stellar disk and dark matter halo density profiles. The hot disk model has a slightly lower f_{disk} value due to its slightly reduced circular speed in the inner region. The rationale behind the hot disk model's lower circular speed is elaborated in Section 2.1 and Figure 1 of [Paper I](#).

With f_{disk} being very similar among the models, the Toomre Q parameter is important in evaluating the stability of the disks. The Q curves show a similar shape across all three disk models but hold different values. The cold, warm, and hot disks exhibit minimum Toomre stability values (Q_{min}) of 0.82, 1.34, and 2.24, respec-

tively. According to the criterion for bar formation in [Jang & Kim \(2023\)](#), the cold disk is susceptible to bar instability, the warm disk is marginally stable, and the hot disk is stable against bar formation. In isolated simulations, the cold and warm disks are capable of spontaneously forming bars, with the warm disk requiring more time to reach a comparable bar strength. The hot disk does not develop a bar within 6 Gyr.

Utilizing these galaxy models, we perform a series of flyby interaction simulations. The perturber in these simulations is a pure Hernquist DM halo composed of live particles. The galaxy and perturber are placed on a hyperbolic orbit, inspired by the configuration presented by [Lokas \(2018\)](#) (refer to her Figure 1 for a schematic). We investigate mass ratios of the perturber to the galaxy ($M_{\text{per}}/M_{\text{gal}}$) of 1/1, 1/3, and 1/10, resulting in strong, moderate, and weak tidal perturbations, respectively. For each mass ratio, we adjust the inclination angle between the stellar disk plane and the perturber's orbit plane to simulate prograde (0°), perpendicular (90°), and retrograde (180°) flyby interactions. The closest approach is set to occur at approximately $t_{\text{peri}} = 0.5$ Gyr for all flyby simulations.

Each simulation is evolved for 6 Gyr with **GADGET-4** ([Springel 2005](#); [Springel et al. 2021](#)). We populate the stellar disk with 0.5 million particles and the galaxy DM halo with 1 million particles, leading to particle masses of $7.2 \times 10^4 M_\odot$ for the disk and $3.6 \times 10^5 M_\odot$ for the halo. The gravitational softening lengths are set at 23 pc for stars and 57 pc for DM particles. We acknowledge that the mass resolution of our simulations is not exceptionally high, yet it is adequate to capture the growth of the bar. [Dubinski et al. \(2009\)](#) demonstrated that the evolution of the bar exhibits convergent behavior when the number of halo particles ranges from 1 million to 10 million. This convergence is evident when studying bar growth, pattern speed evolution, the dark matter halo density profile, and the nonlinear analysis of orbital resonances.

3. BAR GROWTH TIMESCALE

The bar strength A_2 is measured as the amplitude of the $m = 2$ Fourier mode of the stellar disk. We first calculate the sine and cosine coefficients for the stellar disk:

$$a_2 = \frac{\sum_{i=1}^N m_i \cos(2\phi_i)}{\sum_{i=1}^N m_i}, \quad (2a)$$

$$b_2 = \frac{\sum_{i=1}^N m_i \sin(2\phi_i)}{\sum_{i=1}^N m_i}, \quad (2b)$$

where m_i and ϕ_i represent the mass and the azimuthal angle of the i -th particle, respectively. The summation is

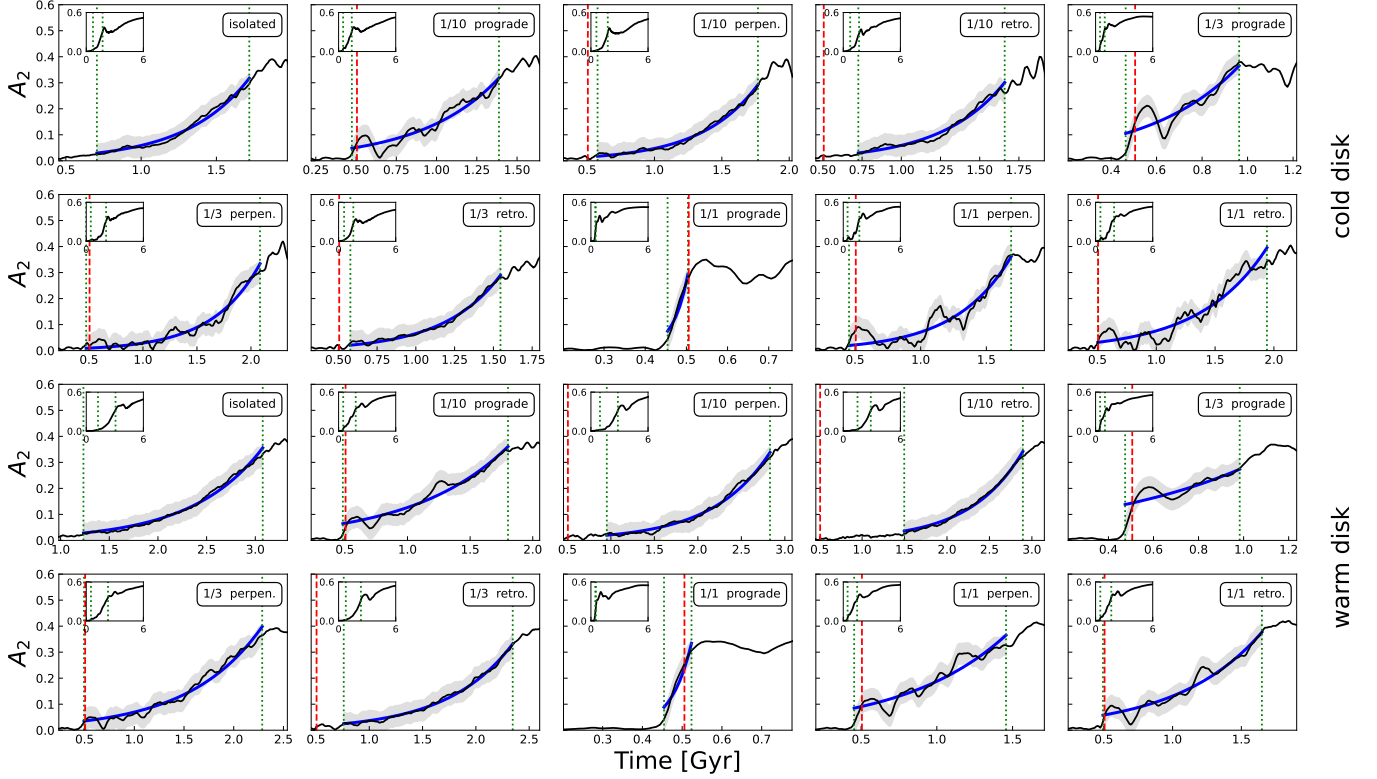


Figure 1. Exponential fitting to the A_2 growth. The black solid lines represent the evolution of A_2 , with the 1σ range highlighted by the grey area. The blue solid lines indicate the results of the exponential fitting. The regions selected for fitting are denoted by green vertical dotted lines, while the intended pericenter time, $t_{\text{peri}} = 0.5$ Gyr, is marked by red vertical dashed lines. The inset axes display the A_2 evolution across the entire simulation duration of 6 Gyr. The text box notes the simulation information of mass ratio ($M_{\text{per}}/M_{\text{gal}} = 1/10, 1/3$, and $1/1$) and orbit type (prograde, perpendicular, and retrograde).

conducted over the stellar particles within a cylindrical region where $R \leq 4 R_d$, i.e., $R \leq 8$ kpc in our galaxy models. The bar strength A_2 is then calculated as:

$$A_2 = \sqrt{a_2^2 + b_2^2}. \quad (3)$$

After (Bland-Hawthorn et al. 2023), we fit the A_2 evolution with an exponential function:

$$A_2(t) = 0.1 \exp((t - t_0)/\tau_{\text{bar}}) \quad (4)$$

to obtain the growth timescale τ_{bar} and the time when A_2 reaches 0.1 (noted as t_0). τ_{bar} characterizes the growth rate of the bar structure, while t_0 reflects the onset time of bar formation. We note that the exact choice of A_2 threshold for t_0 should be high enough to avoid noise but low enough to capture the early phase of bar formation. Equation 4 is equivalent to a simple exponential growth model:

$$A_2 = C \exp(t/\tau_{\text{bar}}), \quad (5)$$

where $C = 0.1 \exp(-t_0/\tau_{\text{bar}})$. When applying to the same data set, both fitting functions yield the same value and the same standard deviation error of the growth

timescale τ_{bar} . Neither function is better than the other, but we prefer Equation 4 for fitting the A_2 evolution due to the slightly better physical interpretability of t_0 compared to C . Besides, the t_0 parameter assists in indicating the initiation time of bar formation, which is beneficial when comparing bar formation scenarios with similar τ_{bar} values. This is helpful when comparing tidally forced bars with the bars formed in isolated simulations within the same disk model as discussed in section 4. We explored other fitting functions in Appendix A. These different functions yield similar τ_{bar} values with differences of approximately 20% while maintaining equivalent fitting quality.

We perform the fitting with the Levenberg–Marquardt algorithm through the `curve_fit` function in the `scipy.optimize` package (Virtanen et al. 2020), following the same method as Bland-Hawthorn et al. (2023). The fitting range starts when the bar strength reaches $A_2 = 0.025$ and ends when A_2 reaches $0.8 A_{2,\text{peak}}$ with $A_{2,\text{peak}}$ being the peak A_2 value during the bar forma-

tion stage.¹ This lower limit is chosen to avoid initial stages when A_2 cannot be well decided. The upper limit is set to avoid the saturation of the bar strength at which the bar growth deviates from the exponential profile. We manually introduce a constant error² of $\sigma_{A_2} = 0.04$ to the A_2 values to account for noise and to calculate the 1σ error of the fitting parameters.

Our fitting results are presented in Figure 1. The majority of the simulations show exponential growth profiles of the bar strength with the fitting results well overlapping the A_2 evolution, consistent with the swing amplifier feedback loop theory. However, several simulations show a deviation from this exponential growth, predominantly occurring in prograde interactions with massive perturbers. Visual examination of the stellar surface density maps reveals that this deviation is primarily due to the substantial contribution of spiral arms to the A_2 signal. We provide more details regarding our fitting method and further demonstrate its reliability in Appendix A.

4. RESULTS & DISCUSSIONS

4.1. Do tidal bars grow faster?

Tidal interactions can either promote or delay bar formation. In this section, we investigate how external perturbations influence the growth of bar structures by comparing the growth timescale τ_{bar} and the onset time t_0 of bar formation between tidally forced and internally developed bars within the same disk.

The comparison is presented in Figure 2 with the *left column* for the cold disk and the *right column* for the warm disk. The upper panels show that the tidally forced bars exhibit τ_{bar} comparable to that of the internally developed bars in the same disk. In most cases, the discrepancy is less than 20%. Considering that different fitting functions can yield τ_{bar} differences of approximately 20%, our result suggests that tidal bars share similar growth rates with their spontaneous counterpart in the same disk. Additionally, the relatively small standard deviation of τ_{bar} indicates that the fitting results are robust against noise in the A_2 evolution.

The largest discrepancy in τ_{bar} is observed in prograde interactions with a mass ratio of 1/1. In such cases, the perturbation is sufficiently strong to generate prominent spiral arms that significantly contribute to the A_2 signal. This situation reduces the reliability of the fitted

τ_{bar} as it no longer exclusively represents the growth of the bar structure. Bland-Hawthorn (*in prep.*, private communication) reports bars and spiral arms may be separated by radial actions. However, it is beyond the scope of this study to disentangle the contribution of the spiral arms to the A_2 signal from the bar growth. Therefore, we conclude that tidally forced bars grow as fast as their spontaneous counterpart in the same disk while acknowledging the potential influence of spiral arms on the A_2 signal.

In the lower panels of Figure 2, we present the fitted t_0 , the time at which the fitted A_2 profile reaches 0.1. Tidally forced bars have an earlier onset of formation, as indicated by their smaller t_0 values. The onset of bar formation occurs earlier with stronger tidal perturbations. The only exception happens in the perpendicular interaction of cold disk with perturber of $M_{\text{per}}/M_{\text{gal}} = 1/3$, where bar formation is delayed by ~ 0.4 Gyr. The underlying cause of the delay will be explored in subsection 4.2.

In the cold disk model (*lower left panel*), the prograde interactions exhibit significantly smaller t_0 values compared to the isolated case, whereas the perpendicular and retrograde interactions show similar t_0 values. These results indicate that bar formation in the cold disk is predominantly driven by internal disk instability, with only severe external perturbations capable of accelerating the emergence of bars.

In the warm disk model (*lower right panel*), all interactions result in smaller t_0 values compared to the isolated case except for the weakest interactions with $M_{\text{per}}/M_{\text{gal}} = 1/10$ on perpendicular and retrograde orbits. The warm disk is only marginally stable against bar formation in isolation. In its interaction simulations, bar formation is a product of the combination of both internal disk instability and external perturbations.

Figure 2 illustrates that tidal interactions promote/delay bar formation by either advancing/postponing the onset of this process. Following the onset of bar formation, tidally forced bars grow at a rate comparable to internally developed bars within the same disk. This conclusion is further reinforced by Figure 3, where we plot the A_2 evolution against $(t - t_0)$. All tidally forced bars exhibit similar growth patterns when referenced against the isolated case, regardless of whether the tidal perturbation accelerates or postpones bar formation. The only notable deviation occurs in prograde interactions with massive perturbers, where the contribution of spiral arms to A_2 is significant. In such scenarios, the tidal force exerted by the perturber impacts stars in the prograde disk for a longer duration than those in the perpendicular or retrograde disk,

¹ Only the bar formation stage before the bar buckling phase is considered for the fitting. The secular growth stage after buckling is excluded.

² The exact value of σ_{A_2} is not crucial as long as it is reasonably chosen to avoid unrealistic impact on the fitting results.

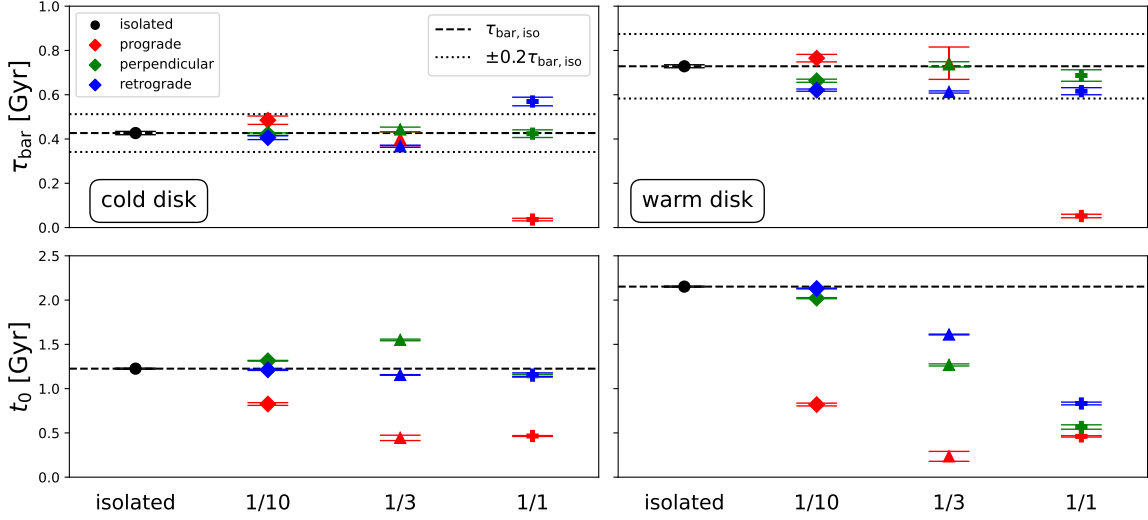


Figure 2. Results of the exponential fitting for the cold disk model (*left column*) and the warm disk model (*right column*). Each scatter point represents a simulation and the error bar shows the standard deviation on the parameter estimate. The dashed lines indicate the results for the same disk model in isolation. *Upper panels:* the growth timescale τ_{bar} . Tidally forced bars exhibit τ_{bar} values similar to those of internally developed bars, with an offset of less than 20%, suggesting that tidal bars and spontaneous bars in the same disk have comparable growth rates. *Lower panels:* the fitted t_0 , representing the time at which A_2 reaches 0.1. Tidal perturbations promote bar formation by advancing the onset time, as evidenced by their smaller t_0 values.

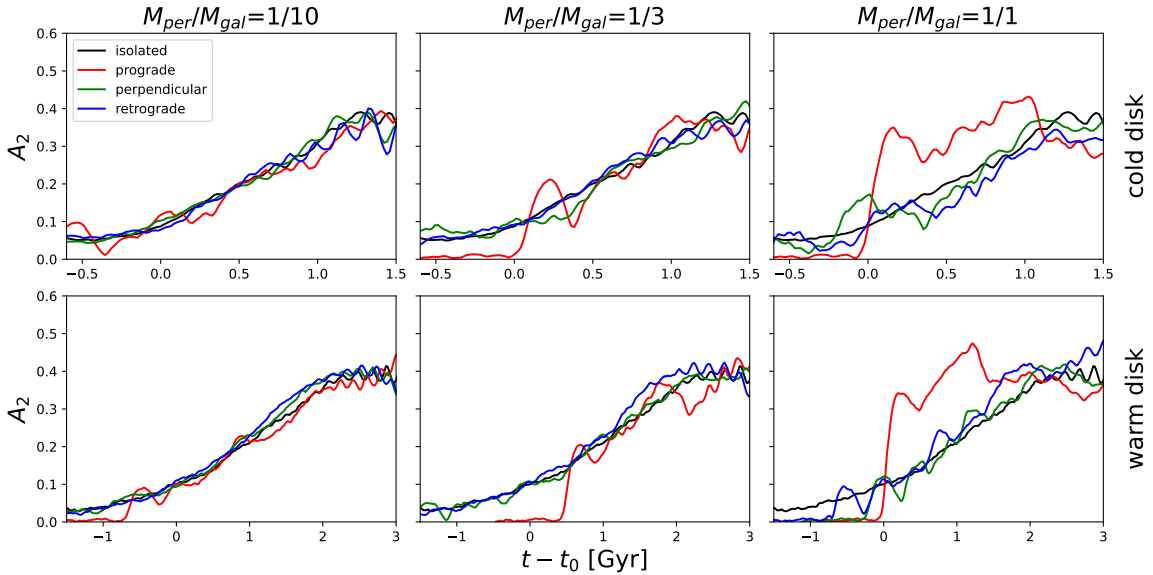


Figure 3. The A_2 evolution against $(t - t_0)$. All tidally forced bars, except those in prograde interactions (red lines) with massive perturbers where spiral arms significantly contribute to the A_2 signal, exhibit growth patterns very similar to the isolated case. This similarity confirms that tidal bars share comparable growth rates with their spontaneous counterparts in the same disk.

thereby promoting the development of spiral arms. We refer the reader to [Lokas \(2018\)](#) and [Paper I](#) for more discussion on the effect of the inclination of the perturber orbit.

The consistency in τ_{bar} suggests that the growth of tidal bars is predominantly governed by the inherent nature of the galaxy, which remains largely unaffected by the tidal perturbation. Tidal perturbations do not substantially alter the swing amplification process, although they provide stronger initial noises that trigger the swing amplification loop. Tidally forced bars grow as fast as their spontaneous counterpart in the same disk.

Our results suggest the fundamental mechanism driving bar growth in cold and warm disks may still be their internal bar instability even under tidal perturbations. The external perturbation mainly affects the onset of the bar formation. Bars formed under tidal interactions in these disks are not purely tidally forced but rather a result of both internal instability and external perturbation. For convenience, we continue to use the term “tidally forced bars” loosely throughout this paper.

These results concerning the **growth timescale comparison** align with the findings in [Paper I](#), where we reached the same conclusion through a **pattern speed comparison**. [Paper I](#) showed that tidally forced bars rotate at speeds comparable to those of internally developed bars within the same disk when bar strength and/or length are taken into account. Both [Paper I](#) and this work suggest that tidal perturbations influence the bar’s evolution by advancing or delaying it to a different stage, but they do not modify the bar’s intrinsic properties or underlying formation mechanism.

Note that τ_{bar} is not precisely identical between tidally forced bars and internally developed ones. We propose two potential factors for this minor discrepancy. One is the transient spiral arms that contribute to the A_2 signal with the extreme cases being those of the prograde interactions with a mass ratio of 1/1. The other factor is the effect of the DM halo spin. Although the primary galaxy’s halo is initially set up without net angular momentum, the tidal force from the perturber spins it up. Isolated simulations have demonstrated the significance of inner halo angular momentum in bar formation: bars grow more rapidly in prograde halos while more slowly in counter-rotating halos (see e.g. [Collier & Madigan 2021](#); [Kataria & Shen 2022](#); [Joshi & Widrow 2024](#)). Observations also suggest a relationship between bar structures, dark matter halo mass/spin, and galaxy mass/spin ([Romeo et al. 2023](#)). The counter-rotating halo spin may explain why the retrograde 1/1 interaction of the cold disk has a larger τ_{bar} .

Although likely a secondary factor, the spinned-up halo does contribute to bar formation. A detailed examination of the halo spin effect in interactions will be addressed in subsequent papers of this series.

4.2. How perturbation affects the onset of the bar formation

Although the perturbation does not alter the bar growth rate, it plays a crucial role in triggering bar formation. In most of our cases, the perturber promotes the onset of bar formation. Following the works of [Dubinski et al. \(2008\)](#), [Polyachenko \(2016\)](#), and [Moetazedian et al. \(2017\)](#), we investigate how interactions influence the onset of bar formation by examining the perturbation waves.

We analyze the flyby interaction of the warm disk model under an intermediate perturbation ($M_{\text{per}}/M_{\text{gal}} = 1/3$, perpendicular orbit), in which the bar formation is advanced by 0.7 Gyr. The onset of the large-scale bar-like perturbation in this case is presented in [Figure 4](#). The left column shows the stellar surface density maps. The right three columns illustrate the deviations between the current snapshot and the initial condition, specifically in terms of stellar surface density ($\Delta\Sigma$), averaged radial velocity ($\Delta\langle V_R \rangle$), and averaged azimuthal velocity ($\Delta\langle V_\phi \rangle$), respectively. We note that the average radial velocity of the axisymmetric disk at the beginning of the simulation is zero. Thus, $\Delta\langle V_R \rangle = \langle V_R \rangle$.

The first row depicts a time shortly after the perturber’s closest approach. The interaction triggers a perturbation wave that propagates to the galaxy’s center. This wave generates a “seed bar”, as indicated by the quadrupole signal in the velocity fields shown in the second row. Subsequently, the swing amplification feedback loop amplifies this seed bar into a robust bar structure. We illustrate the bar’s evolution at t_0 , i.e., the time when A_2 reaches 0.1, in the third row. The final row displays the bar at a later stage when A_2 reaches 0.2, a common criterion for identifying strong bars.

To further confirm the link between the perturbation and the onset of the bar formation, we rerun several flyby simulations of the warm disk with the pericenter time being delayed by 1 Gyr. As expected, the bar formation is delayed by a similar amount compared with the original runs, as revealed by the t_0 parameter.

For comparison, we present the onset of bar formation in the same disk evolved in isolation in [Figure 5](#). A similar quadrupole signal in the velocity fields spontaneously emerges at the galaxy center as shown in the first row. However, the “seed bar” appears 0.7 Gyr later compared to the flyby interaction scenario shown in [Fig-](#)

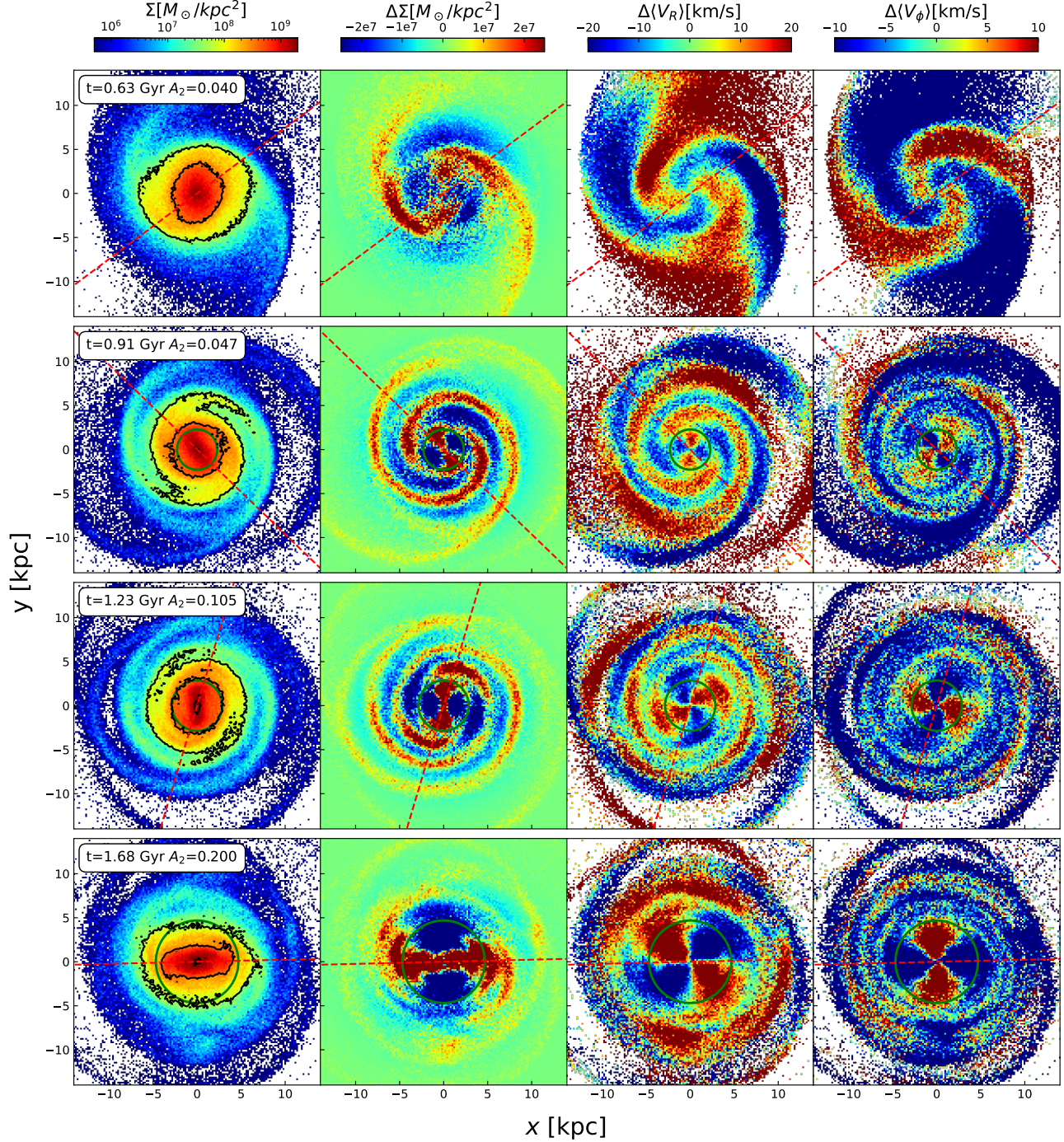


Figure 4. The onset of a large-scale bar-like perturbation during a flyby interaction (warm disk, $1/3$, perpendicular orbit). The left column displays the stellar surface density maps with the time and A_2 amplitude indicated in the text box. The right three columns show the differences between the current snapshot and the initial condition in terms of stellar surface density ($\Delta\Sigma$), averaged radial velocity ($\Delta\langle V_R \rangle$), and averaged azimuthal velocity ($\Delta\langle V_\phi \rangle$), respectively. The rows present a temporal evolution from top to bottom. In the first row, the tidal perturbation wave propagates to the galaxy center shortly after the perturber’s pericenter passage. This wave initiates a “seed bar” as shown by the quadrupole signal in the velocity fields (outlined by green circles) in the second row. The third and fourth rows illustrate the bar’s evolution at times when A_2 reaches 0.1 and 0.2, respectively. In each panel, the ϕ angle of the A_2 signal is marked with a red dashed line.

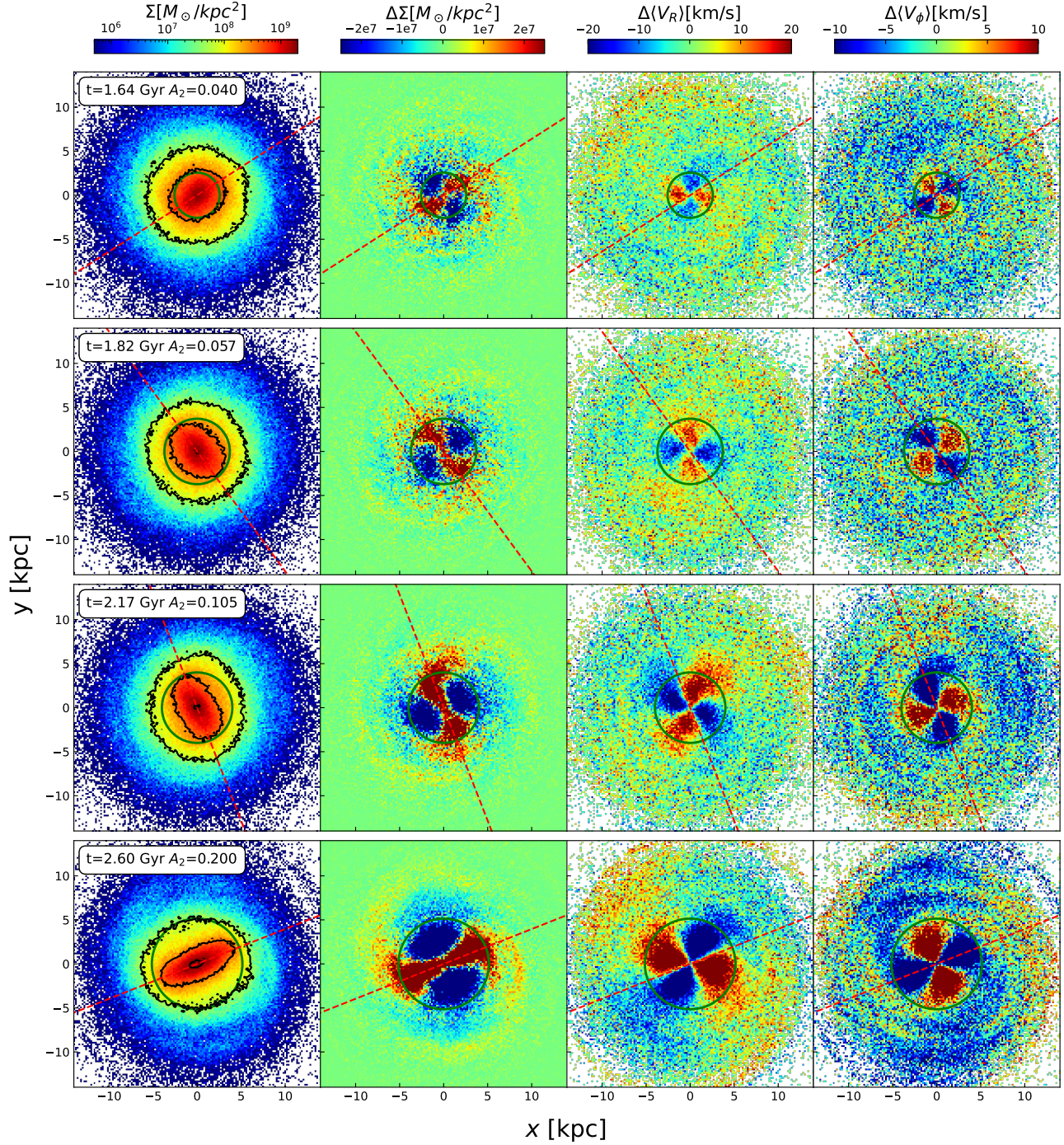


Figure 5. Same as Figure 4 but for the same disk evolved in isolation. The “seed bar” spontaneously emerges at the galaxy center and gradually evolves into a strong bar structure. The “seed bar” emerges ~ 0.7 Gyr later than the flyby interaction case shown in Figure 4.

ure 4. The bottom three rows of Figure 5 illustrate the development of the “seed bar” into a strong bar structure. The evolution of the bar in the isolated case is similar to that under tidal perturbation (Figure 4) except for the stronger spiral arms in the latter case. This consistent evolution further supports the notion that the tidal bar grows at a rate comparable to its spontaneous counterpart in the warm disk.

Tidal perturbations can also postpone the onset of bar formation. Figure 6 illustrates a delayed scenario in the cold disk model ($M_{\text{per}}/M_{\text{gal}} = 1/3$, perpendicular orbit). The first row shows a moment shortly before the perturber’s closest approach. Although weak, the cold disk has already spontaneously generated a “seed bar” prior to the interaction. When the perturbation wave reaches the galaxy center, it interferes destructively with the original seed bar and limits the bar’s growth. Ultimately, one mode prevails over the other at a later time and starts the steady growth of the bar as seen in the bottom row ($A_2 = 0.1$). We propose that the internal mode dominates over the external mode as the perturber is already more than $300 R_d$ away when A_2 reaches 0.1.

Our results align with the interpretation of Moetazedian et al. (2017) regarding the delayed case. Destructive interference is due to the external perturbation wave being **accidentally** out of phase with the internally developed seed bar when it reaches the galaxy center. We test this hypothesis by re-simulating the delayed case with slightly altered pericenter times, shifted by ± 0.1 Gyr. In both the earlier and later interactions, the onset of bar formation is advanced by approximately 0.2 Gyr compared to the isolated cases, rather than being delayed as in the original interaction. This result underscores the difficulty for tidal perturbations to delay bar formation within galaxies inherently susceptible to internal instability, thereby explaining why the majority of our interaction simulations have earlier emergences of bars. Tidal perturbations provide stronger initial noises for the swing amplification feedback loop, while the probability of the external perturbation wave being out of phase with the internally developed seed bar is indeed small. Our results also highlight the complexity of predicting the galaxy morphology, which is influenced by both their environment and internal baryonic physics (Zhou et al. 2020).

4.3. bar growth in hot disk model

In a more specific context, the term “tidally forced bars” refers exclusively to bars in galaxies that are stable against bar formation when isolated. Consequently, we examined bar growth in the hot disk model, which avoids bar instability throughout a 6 Gyr isolated evolution.

We utilize the **same exponential fitting (Equation 4)** for the A_2 evolution in the hot disk model. Since A_2 does not exhibit a distinct peak in the hot disk, we extend the upper limit of the fitting time range to the end of the simulation, i.e., 6 Gyr. For the lower limit, we set $A_2 > 0.025$ and exclude the initial 0.75 Gyr of the simulation. Visual examination of the stellar surface density indicates that the significant increase in the A_2 signal around the interaction time ($t_{\text{peri}} = 0.5$ Gyr) is primarily due to overall distortion of the disk and transient spirals, rather than bar formation. The fitting outcomes are presented in Figure 7. Unlike the cold and warm disks, the hot disk does not display a consistent τ_{bar} , ranging from a minimum of 1.85 Gyr to a maximum of 6.11 Gyr. Notably, the $M_{\text{per}}/M_{\text{gal}} = 1/1$ interactions yield larger τ_{bar} values compared to the interactions with less massive perturbers, even though the bars in the former cases are stronger. When $M_{\text{per}}/M_{\text{gal}}$ is fixed, the τ_{bar} values are larger for bars developed under prograde interactions compared to those that form under perpendicular and retrograde interactions. Since perturbers on prograde orbit provide stronger perturbations compared to those in perpendicular or retrograde orbit (see Lokas 2018 and Sec 4.2 of Paper I), this result also implies that stronger perturbations result in larger τ_{bar} values. We suggest that τ_{bar} of the tidally forced bar qualitatively correlates with the strength of the perturbation and leave the quantification of the correlation for further investigation in the future.³

The growth of A_2 in the hot disk does not adhere to a clear exponential pattern, unlike in the cold and warm disks. In addition to exponential fitting, we also utilize the following linear fitting to model the evolution of A_2 in the hot disk model:

$$A_2(t) = kt + b, \quad (6)$$

where k represents the linear growth rate of the bar strength. The linear fitting is also presented in Figure 7 with the k values noted in the text box. Similar to the result in τ_{bar} , we find a qualitative relation that stronger interactions correspond to larger k values, suggesting the correlation between interaction strength and bar growth in the hot disk.

Visually, the linear function seems to offer a slightly better fit to the growth of tidally forced bars in the hot

³ One way to measure the perturbation strength by the dimensionless tidal strength parameter S introduced in Elmegreen et al. (1991). We found that S is approximately 0.87, 0.15, and 0.03 for $M_{\text{per}}/M_{\text{gal}} = 1/1$, $1/3$, and $1/10$ respectively. However, S does not take into account the inclination of the perturber’s orbit that also affects the strength of tidal interaction (see Lokas 2018 and Sec 4.2 of Paper I).

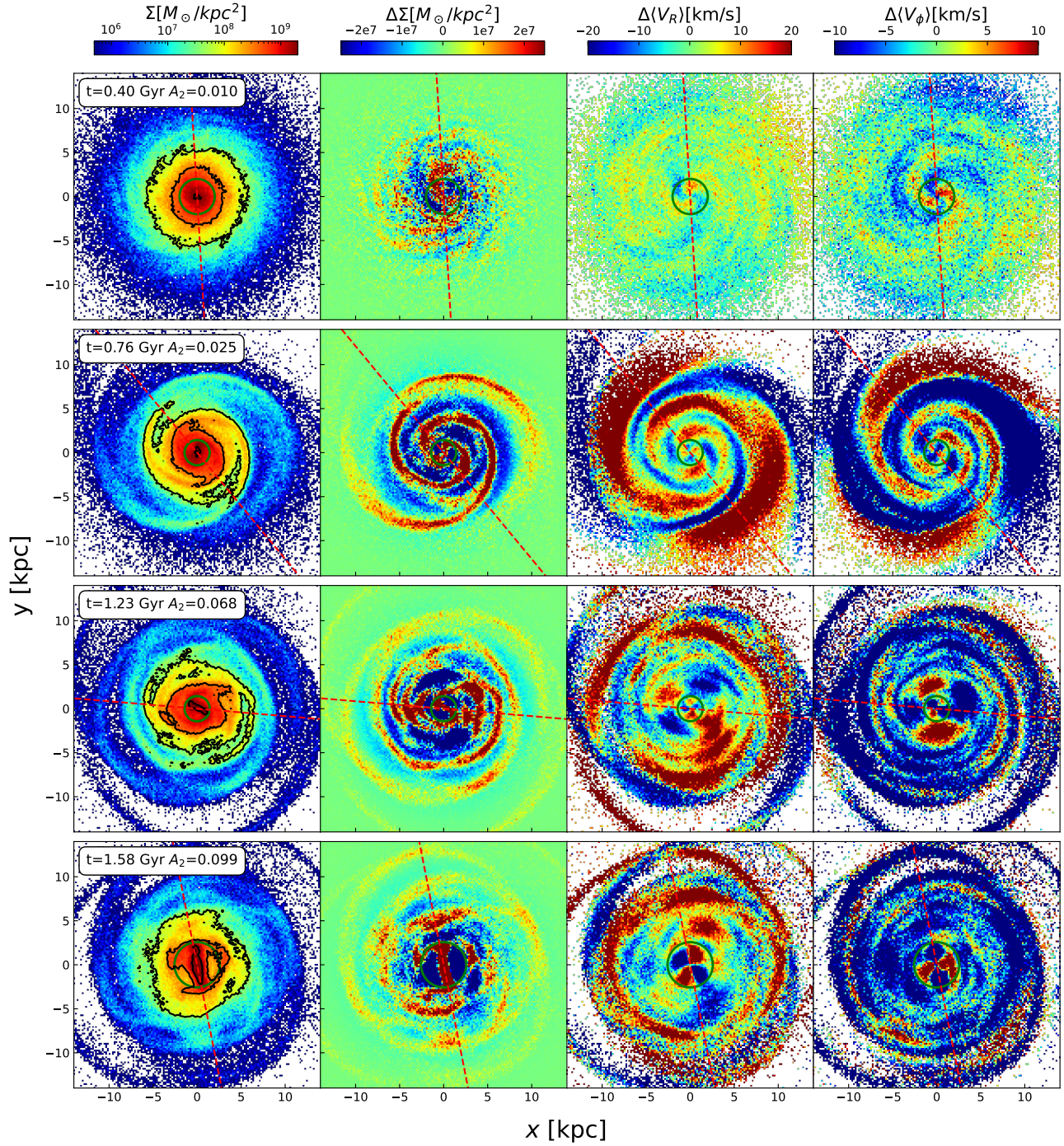


Figure 6. Same as Figure 4 but for a delayed case (cold disk, 1/3, perpendicular). Although weak, the cold disk spontaneously generates a “seed bar” prior to the interaction (top row). When the perturbation wave reaches the galaxy’s center, it is out of phase with the pre-existing seed bar, causing destructive interference and limiting the bar’s growth (middle two rows). Despite this initial delay, the bar eventually resumes steady growth at a later stage (bottom row).

disk for most scenarios. From a statistical perspective, the linear fit yields a smaller reduced chi-squared statistic (χ^2_ν) compared to the exponential fit. Conversely, the cold and warm disks exhibit a more favorable fit with the exponential function during the bar formation phase. The linear fitting approach may be more appropriate for describing the secular evolution of the bar in the cold and warm disks, occurring after the buckling stage and prior to the saturation stage (refer to the inset axes in Figure 1, and also Figure 4 in Paper I).

The linear growth can be interpreted as an approximation of exponential growth with a large timescale. If a series of models of increasing stability is simulated, it is expected that the increasing τ_{bar} will gradually transition the bar growth from exponential to linear. Therefore, the slight preference for linear bar growth alone is insufficient to serve as decisive evidence that tidally forced bars in the hot disk model are fundamentally different from those developed in the cold and warm disks.

However, we emphasize an important fact that both the exponential and linear growth rates of the tidally forced bars in the hot disk correlate with the perturbation strength. It contrasts with the consistent growth rate of bars within cold or warm disks, where bar growth is primarily driven by internal disk instability. This difference makes it less meaningful to compare the growth timescale τ_{bar} between the hot disk and the cold/warm disks. It also suggests that bars in the hot disk may not operate under the swing amplification mechanism, contrasting with those in the cold and warm disks. Possibly, the hot dynamical state of the disk resists the disturbance caused by the perturber, preventing the disruption of the galaxy center and rendering it less susceptible to the swing amplification feedback loop (Dubinski et al. 2008).

We examine the velocity fields of the bars within the hot disk model and observe that the quadrupole signal is more extended but weaker compared to bars in the cold and warm disks with similar bar strength. Bars in hot disks are also longer and less eccentric at the same A_2 . Their subsequent evolution encompasses both the elongation of the bar and the increase in eccentricity.

If the term “tidally forced bars” is strictly applied to those in galaxies that inherently avoid bar instability, their formation and evolution differ from those in galaxies that are prone to bar instability. Quantitative comparison of bar shapes and dynamical/kinematical analysis of the bar regions have the potential to distinguish these two categories of bars. This will constitute the long-term objective of this series of papers.

5. SUMMARY

We employ a suite of controlled N -body simulations to investigate the growth of bars under both tidally forced and internally developed mechanisms. We generate three pure disk galaxy models with varying stabilities against bar formation by adjusting the radial velocity dispersion. The models are labeled cold, warm, and hot. The cold and warm disk models spontaneously form bars, although the warm one takes a longer time to do so. The hot disk model does not develop a bar within 6 Gyr of isolated evolution. We then introduce a perturber to induce tidal interactions with mass ratios of 1/1, 1/3, and 1/10 and inclination angles of 0° , 90° , and 180° relative to the disk plane.

We apply an exponential fitting to the A_2 evolution in cold and warm disks to quantify the growth timescale τ_{bar} and the onset time t_0 of the bar formation (Figure 1). The tidally forced bars show similar τ_{bar} to that of the internally developed bars with differences less than 20%, indicating that tidal bars have similar growth rates to their spontaneous counterpart in the same disk (Figure 2). The tidal perturbation promotes/delays the bar formation by advancing/postponing the onset time t_0 . This conclusion is further corroborated by comparing the A_2 evolution against $(t - t_0)$. (Figure 3). If the disk inherently possesses instability, the primary driver of bar formation is its internal nature that remains largely unaffected by tidal perturbations.

We further investigate the onset of the bar formation by examining the perturbation wave. In instances where the perturbation advances bar formation, the perturbation wave propagates the galaxy center shortly after the perturber’s pericenter and evokes a “seed bar” (Figure 4). The isolated case shows a similar evolution of the “seed bar” but its spontaneous emergence occurs approximately 0.7 Gyr later than in the interaction case (Figure 5). We also show a delayed interaction case where the perturbation wave is out of phase with the internally developed seed bar, leading to destructive interference and limiting the growth of the bar (Figure 6).

In the hot disk model, the tidally forced bars do not show consistent τ_{bar} values (Figure 7), probably due to the deviation from the exponential growth profile. The linear fitting provides a slightly better description of the bar growth in the hot disk than the exponential fitting. These results make it less meaningful to compare the growth timescale τ_{bar} between the hot disk and the cold/warm disks and hints that bars in the hot disk may not follow the same growth mechanism as those in the cold and warm disks.

However, the difference in the bar growth mechanisms holds the potential to separate tidally forced bars that developed in stable galaxies from those developed in

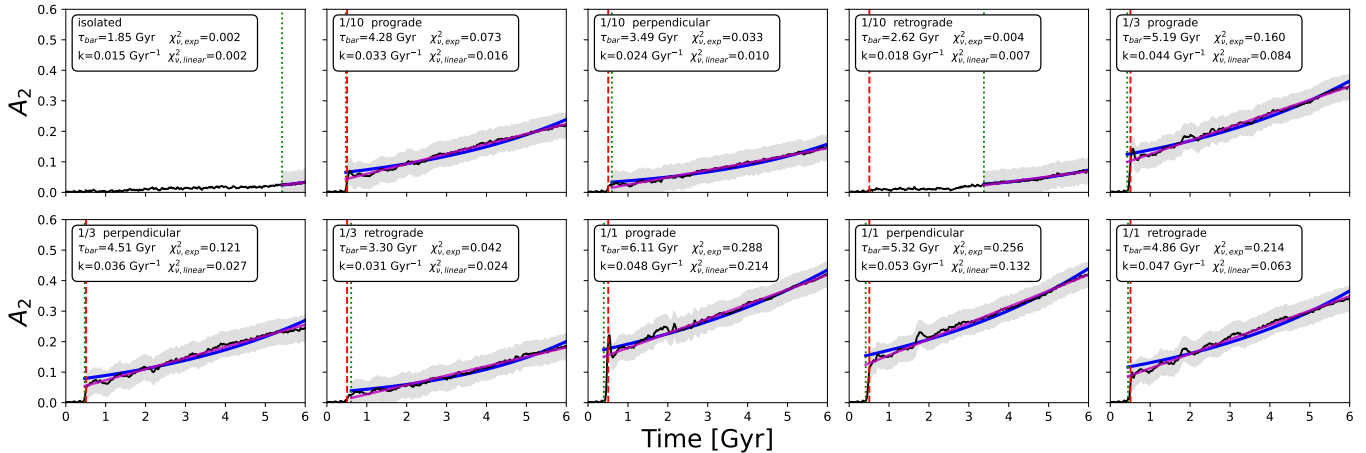


Figure 7. Similar to Figure 1 but for the hot disk model. The magenta lines show the linear fitting results. The text box provides the simulation information alongside the exponential growth timescale τ_{bar} and the linear growth rate k . χ^2_{ν} of different fittings are also noted. Unlike the cold and warm disks, the hot disk does not show consistent τ_{bar} values.

galaxies that are inherently susceptible to bar instability. Further investigation of the bar’s shape and dynamical/kinematical analysis of the bar regions could be important in distinguishing between these two types of bars.

With the advent of powerful telescopes, such as the Atacama Large Millimeter Array (ALMA) and the James Webb Space Telescope (JWST), astronomers can now observe the gas-rich phase of galaxies at high redshifts. Considering that all disk galaxies undergo a gas-rich phase, the new era of gas-rich controlled simulations is vital for further insights into the bar formation mechanism (Bland-Hawthorn et al. 2024, 2025). We will explore the impact of gas on bar formation and evolution under both the internal and external formation mechanisms in future work.

Software: AGAMA (Vasiliev 2019), GADGET-4 (Springel 2005; Springel et al. 2021), NumPy (Harris et al. 2020), SciPy (Virtanen et al. 2020), Matplotlib (Hunter 2007), Jupyter Notebook (Kluyver et al. 2016)

ACKNOWLEDGEMENTS

We thank the referee for suggestions that helped to improve the presentation of the paper. We thank Thor Tepper-Garcia and Joss Bland-Hawthorn for their help with the AGAMA work and with initializing the galaxy models. We thank Zhi Li and Sandeep Kumar Kataria for their valuable insights on simulations and analysis. We also thank Rui Guo for their helpful discussions. The research presented here is partially supported by the National Key R&D Program of China under grant No. 2018YFA0404501; by the National Natural Science Foundation of China under grant Nos. 12025302, 11773052, 11761131016; by the “111” Project of the Ministry of Education of China under grant No. B20019; and by the Chinese Space Station Telescope project. J.S. acknowledges support from the *Newton Advanced Fellowship* awarded by the Royal Society and the Newton Fund. X.W. wishes to thank the financial support from the Natural Science Foundation of China (Numbers NSFC-12073026, NSFC-12433002). This work made use of the Gravity Supercomputer at the Department of Astronomy, Shanghai Jiao Tong University.

APPENDIX

A. FITTING VALIDATION

In addition to Equation 4, we explored alternative exponential formulas to fit the A_2 evolution. One such formula is:

$$A_2(t) = C_1 \exp(t/\tau_{\text{bar}}) + C_2, \quad (\text{A1})$$

which offers greater flexibility in the fitting process. We also examined the following formula:

$$A_2(t) = C(\exp(t/\tau_{\text{bar}}) - 1), \quad (\text{A2})$$

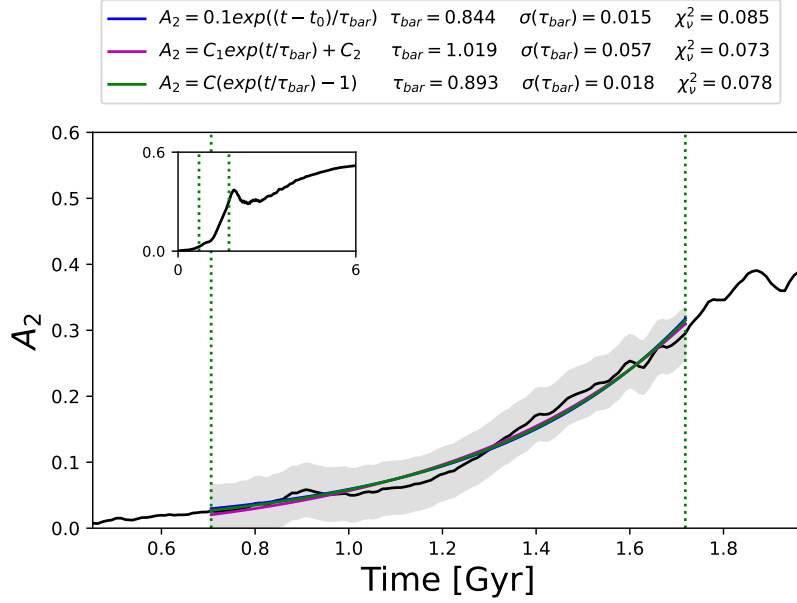


Figure A1. Results of exponential fitting using different formulas for the isolated evolution of the cold disk. The legend notes the formulas used, the growth timescale τ_{bar} , the 1σ error, and the reduced chi-squared statistic χ^2_{ν} . Different formulas yield similar τ_{bar} with a difference $\sim 20\%$ while having the same “goodness” of fitting as shown by the fitted lines and the similar values of χ^2_{ν} .

This choice is driven by the consideration that the bar strength $A_2 \approx 0$ at $t = 0$ if the disk is set to be perfectly axisymmetric at the beginning of the simulations, even though A_2 is not expected to stay at 0 for a long time.

We employ the same fitting procedure outlined in Section 3 with these alternative formulas to fit the A_2 evolution of the internally developed bar in the cold disk model. The results are presented in Figure A1. Despite employing different formulas, the fits exhibit a similar “goodness”, as indicated by the fitted lines and the comparable χ^2_{ν} . The growth timescales τ_{bar} derived from these formulas are also similar, with differences of $\sim 20\%$. Consequently, we consider a difference of $\sim 20\%$ in τ_{bar} to be acceptable.

To further demonstrate the reliability of the exponential fitting, we compare the fitted t_0 values with the true t_0 values in Figure A2. The fitted t_0 is defined as the time at which the fitted A_2 profile reaches 0.1, while the true t_0 is the time when the actual A_2 profile attains this value. The majority of the simulations show a nice agreement within ± 0.1 Gyr between fitted and true t_0 . Only 6 simulations show slightly larger offsets, ranging between 0.1 and 0.3 Gyr. This agreement underscores the robustness of the exponential fitting approach.

REFERENCES

- Binney, J. 2020, MNRAS, 496, 767,
doi: [10.1093/mnras/staa1485](https://doi.org/10.1093/mnras/staa1485)
- Bland-Hawthorn, J., Tepper-Garcia, T., Agertz, O., & Federrath, C. 2024, ApJ, 968, 86,
doi: [10.3847/1538-4357/ad4118](https://doi.org/10.3847/1538-4357/ad4118)
- Bland-Hawthorn, J., Tepper-Garcia, T., Agertz, O., & Freeman, K. 2023, ApJ, 947, 80,
doi: [10.3847/1538-4357/acc469](https://doi.org/10.3847/1538-4357/acc469)
- Bland-Hawthorn, J., Tepper-Garcia, T., Agertz, O., et al. 2025, arXiv e-prints, arXiv:2502.01895,
doi: [10.48550/arXiv.2502.01895](https://doi.org/10.48550/arXiv.2502.01895)
- Blitz, L., & Spergel, D. N. 1991, ApJ, 379, 631,
doi: [10.1086/170535](https://doi.org/10.1086/170535)
- Byrd, G. G., Valtonen, M. J., Sundelius, B., & Valtaoja, L. 1986, A&A, 166, 75
- Collier, A., & Madigan, A.-M. 2021, ApJ, 915, 23,
doi: [10.3847/1538-4357/ac004d](https://doi.org/10.3847/1538-4357/ac004d)
- de Vaucouleurs, G. 1964, in The Galaxy and the Magellanic Clouds, ed. F. J. Kerr, Vol. 20, 195
- Dubinski, J., Berentzen, I., & Shlosman, I. 2009, ApJ, 697, 293, doi: [10.1088/0004-637X/697/1/293](https://doi.org/10.1088/0004-637X/697/1/293)
- Dubinski, J., Gauthier, J. R., Widrow, L., & Nickerson, S. 2008, in Astronomical Society of the Pacific Conference Series, Vol. 396, Formation and Evolution of Galaxy Disks, ed. J. G. Funes & E. M. Corsini, 321,
doi: [10.48550/arXiv.0802.3997](https://doi.org/10.48550/arXiv.0802.3997)

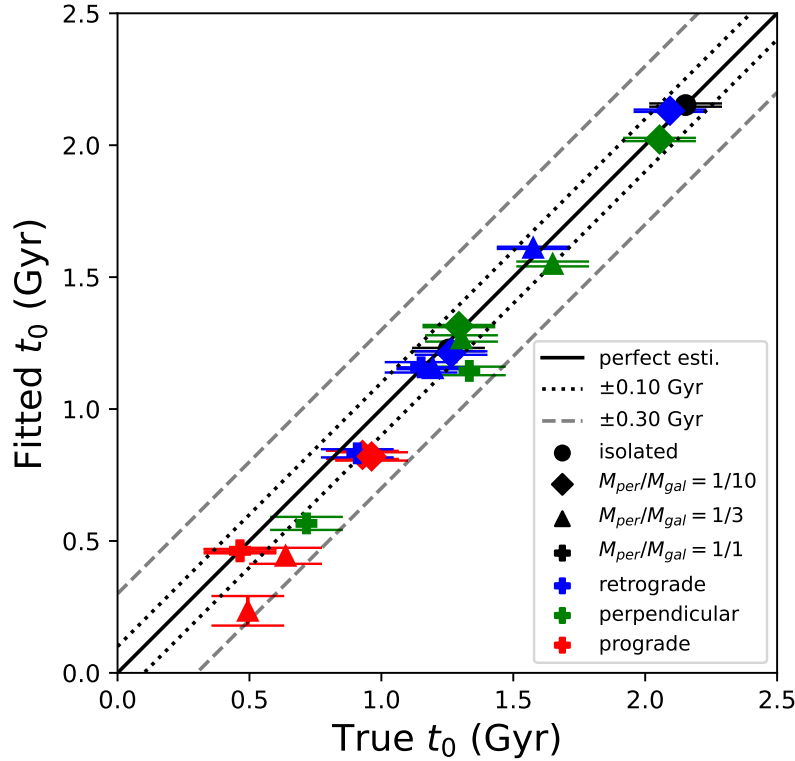


Figure A2. Comparison of the fitted t_0 and true t_0 . Each point represents a simulation, with the shape indicating the mass ratio and the type representing the orbit configuration. The solid diagonal line is the perfect estimation of $t_{0,\text{fit}} = t_{0,\text{true}}$. The dotted and dashed lines mark the offsets of ± 0.1 Gyr and ± 0.3 Gyr, respectively. The reasonable agreement between fitted t_0 and true t_0 outlines the reliability of the exponential fitting.

Elmegreen, D. M., Sundin, M., Elmegreen, B., & Sundelius, B. 1991, *A&A*, 244, 52

Erwin, P. 2018, *MNRAS*, 474, 5372, doi: [10.1093/mnras/stx3117](https://doi.org/10.1093/mnras/stx3117)

Fujii, M. S., Bédorf, J., Baba, J., & Portegies Zwart, S. 2018, *MNRAS*, 477, 1451, doi: [10.1093/mnras/sty711](https://doi.org/10.1093/mnras/sty711)

Gauthier, J.-R., Dubinski, J., & Widrow, L. M. 2006, *ApJ*, 653, 1180

Ghosh, S., Fragkoudi, F., Di Matteo, P., & Saha, K. 2023, *A&A*, 674, A128, doi: [10.1051/0004-6361/202245275](https://doi.org/10.1051/0004-6361/202245275)

Goldreich, P., & Lynden-Bell, D. 1965, *MNRAS*, 130, 125, doi: [10.1093/mnras/130.2.125](https://doi.org/10.1093/mnras/130.2.125)

Guo, Y., Jogee, S., Wise, E., et al. 2024, arXiv e-prints, arXiv:2409.06100, doi: [10.48550/arXiv.2409.06100](https://doi.org/10.48550/arXiv.2409.06100)

Harris, C. R., Millman, K. J., van der Walt, S. J., et al. 2020, *Nature*, 585, 357–362, doi: [10.1038/s41586-020-2649-2](https://doi.org/10.1038/s41586-020-2649-2)

Hohl, F. 1971, *ApJ*, 168, 343

Hozumi, S. 2022, *MNRAS*, 510, 4394, doi: [10.1093/mnras/stab3704](https://doi.org/10.1093/mnras/stab3704)

Hunter, J. D. 2007, *Computing in Science Engineering*, 9, 90, doi: [10.1109/MCSE.2007.55](https://doi.org/10.1109/MCSE.2007.55)

Iles, E. J., Pettitt, A. R., & Okamoto, T. 2022, *MNRAS*, 510, 3899, doi: [10.1093/mnras/stab3330](https://doi.org/10.1093/mnras/stab3330)

Jang, D., & Kim, W.-T. 2023, *ApJ*, 942, 106, doi: [10.3847/1538-4357/aca7bc](https://doi.org/10.3847/1538-4357/aca7bc)

Joshi, R., & Widrow, L. M. 2024, *MNRAS*, 527, 7781, doi: [10.1093/mnras/stad3666](https://doi.org/10.1093/mnras/stad3666)

Julian, W. H., & Toomre, A. 1966, *ApJ*, 146, 810, doi: [10.1086/148957](https://doi.org/10.1086/148957)

Kataria, S. K., & Das, M. 2018, *MNRAS*, 475, 1653, doi: [10.1093/mnras/stx3279](https://doi.org/10.1093/mnras/stx3279)

Kataria, S. K., & Shen, J. 2022, *ApJ*, 940, 175, doi: [10.3847/1538-4357/ac9df1](https://doi.org/10.3847/1538-4357/ac9df1)

Kluyver, T., Ragan-Kelley, B., Pérez, F., et al. 2016, in *Positioning and Power in Academic Publishing: Players, Agents and Agendas*, ed. F. Loizides & B. Schmidt, IOS Press, 87 – 90

Le Conte, Z. A., Gadotti, D. A., Ferreira, L., et al. 2024, *MNRAS*, 530, 1984, doi: [10.1093/mnras/stae921](https://doi.org/10.1093/mnras/stae921)

Lee, Y. H., Ann, H. B., & Park, M.-G. 2019, *ApJ*, 872, 97, doi: [10.3847/1538-4357/ab0024](https://doi.org/10.3847/1538-4357/ab0024)

Li, Z., Shen, J., & Kim, W.-T. 2015, *ApJ*, 806, 150, doi: [10.1088/0004-637X/806/2/150](https://doi.org/10.1088/0004-637X/806/2/150)

- Li, Z.-Y., Shen, J., Bureau, M., et al. 2018, *ApJ*, 854, 65, doi: [10.3847/1538-4357/aaa771](https://doi.org/10.3847/1538-4357/aaa771)
- Lin, L., Li, C., He, Y., Xiao, T., & Wang, E. 2017, *ApJ*, 838, 105, doi: [10.3847/1538-4357/aa657a](https://doi.org/10.3847/1538-4357/aa657a)
- Lin, L., Li, C., Du, C., et al. 2020, *MNRAS*, 499, 1406, doi: [10.1093/mnras/staa2913](https://doi.org/10.1093/mnras/staa2913)
- Lokas, E. L. 2018, *ApJ*, 857, 6, doi: [10.3847/1538-4357/aab4ff](https://doi.org/10.3847/1538-4357/aab4ff)
- . 2019a, *A&A*, 629, A52, doi: [10.1051/0004-6361/201936056](https://doi.org/10.1051/0004-6361/201936056)
- . 2019b, *A&A*, 624, A37, doi: [10.1051/0004-6361/201935011](https://doi.org/10.1051/0004-6361/201935011)
- Lokas, E. L., Ebrov, I., del Pino, A., et al. 2016, *ApJ*, 826, 227, doi: [10.3847/0004-637X/826/2/227](https://doi.org/10.3847/0004-637X/826/2/227)
- Marinova, I., & Jogee, S. 2007, *ApJ*, 659, 1176, doi: [10.1086/512355](https://doi.org/10.1086/512355)
- Martinez-Valpuesta, I., Aguerri, J. A. L., Gonzlez-Garca, A. C., Dalla Vecchia, C., & Stringer, M. 2017, *MNRAS*, 464, 1502, doi: [10.1093/mnras/stw2500](https://doi.org/10.1093/mnras/stw2500)
- Masters, K. L., Nichol, R. C., Hoyle, B., et al. 2011, *MNRAS*, 411, 2026
- Menndez-Delmestre, K., Sheth, K., Schinnerer, E., Jarrett, T. H., & Scoville, N. Z. 2007, *ApJ*, 657, 790, doi: [10.1086/511025](https://doi.org/10.1086/511025)
- Moetazedian, R., Polyachenko, E. V., Berczik, P., & Just, A. 2017, *A&A*, 604, A75, doi: [10.1051/0004-6361/201630024](https://doi.org/10.1051/0004-6361/201630024)
- Ostriker, J. P., & Peebles, P. J. 1973, *ApJ*, 186, 467
- Pettitt, A. R., & Wadsley, J. W. 2018, *MNRAS*, 474, 5645, doi: [10.1093/mnras/stx3129](https://doi.org/10.1093/mnras/stx3129)
- Polyachenko, E. V. 2016, *Baltic Astronomy*, 25, 288, doi: [10.1515/astro-2017-0132](https://doi.org/10.1515/astro-2017-0132)
- Romeo, A. B., Agertz, O., & Renaud, F. 2023, *MNRAS*, 518, 1002, doi: [10.1093/mnras/stac3074](https://doi.org/10.1093/mnras/stac3074)
- Sellwood, J. 2014, *Reviews of Modern Physics*, 86, 1
- Shen, J., Rich, R. M., Kormendy, J., et al. 2010, *ApJL*, 720, L72, doi: [10.1088/2041-8205/720/1/L72](https://doi.org/10.1088/2041-8205/720/1/L72)
- Springel, V. 2005, *MNRAS*, 364, 1105, doi: [10.1111/j.1365-2966.2005.09655.x](https://doi.org/10.1111/j.1365-2966.2005.09655.x)
- Springel, V., Pakmor, R., Zier, O., & Reinecke, M. 2021, *MNRAS*, 506, 2871, doi: [10.1093/mnras/stab1855](https://doi.org/10.1093/mnras/stab1855)
- Toomre, A. 1981, in *Structure and Evolution of Normal Galaxies*, ed. S. M. Fall & D. Lynden-Bell, 111–136
- Vasiliev, E. 2019, *MNRAS*, 482, 1525, doi: [10.1093/mnras/sty2672](https://doi.org/10.1093/mnras/sty2672)
- Virtanen, P., Gommers, R., Oliphant, T. E., et al. 2020, *Nature Methods*, 17, 261, doi: [10.1038/s41592-019-0686-2](https://doi.org/10.1038/s41592-019-0686-2)
- Worrakitpoonpon, T. 2024, *arXiv e-prints*, arXiv:2412.18098, doi: [10.48550/arXiv.2412.18098](https://doi.org/10.48550/arXiv.2412.18098)
- Zana, T., Dotti, M., Capelo, P. R., et al. 2018, *MNRAS*, 473, 2608, doi: [10.1093/mnras/stx2503](https://doi.org/10.1093/mnras/stx2503)
- Zheng, Y., & Shen, J. 2025, *ApJ*, 979, 60, doi: [10.3847/1538-4357/ad9bae](https://doi.org/10.3847/1538-4357/ad9bae)
- Zhou, Z.-B., Zhu, W., Wang, Y., & Feng, L.-L. 2020, *ApJ*, 895, 92, doi: [10.3847/1538-4357/ab8d32](https://doi.org/10.3847/1538-4357/ab8d32)